

# Broadband Oscillator-Free THz Pulse Generation and Radiation Based on Direct Digital-to-Impulse Architecture

M. Mahdi Assefzadeh, *Student Member, IEEE*, and Aydin Babakhani, *Member, IEEE*

**Abstract**—Broadband 0.03–1.1 THz signal generation and radiation are demonstrated based on an oscillator-free direct digital-to-impulse architecture with a 1.9-ps full width at half maximum and 130-GHz 3-dB bandwidth (BW) (200-GHz 10-dB BW) centered at 160 GHz. The radiated pulse achieves a peak pulse effective isotropic-radiated power of 19.2 dBm and peak pulse-radiated power of 2.6 mW. An ON/OFF impulse-shaping technique is introduced and implemented to suppress undesired ringing and to increase dc-to-radiated efficiency. The frequency-comb spectrum of the radiated pulse train with 5.2-GHz repetition rate is measured up to 1.1 THz. At a distance of 4 cm, the measured received SNR at 1 and 1.1 THz is 28 and 22 dB, respectively. A 1.1-THz tone is measured with a 10-dB spectral width of 2 Hz, demonstrating an extremely narrow spectral line width (two parts per trillion). Time-domain picosecond pulses are characterized using a custom femtosecond-laser-based terahertz time-domain spectroscopy system. Coherent spatial combining from two widely spaced chips is demonstrated. It is shown that the starting time of the radiated pulses is locked to the edge of the input digital trigger with a timing jitter of 270 fs. The chip is fabricated in a 130-nm SiGe BiCMOS process technology.

**Index Terms**—BiCMOS, direct digital-to-impulse (D2I), integrated circuits, on-chip antenna, ON/OFF impulse-shaping technique, picosecond, pulse, SiGe, silicon, terahertz (THz).

## I. INTRODUCTION

IN RECENT years, there has been a growing interest in the generation and radiation of ultra-short pulses in the millimeter-wave and terahertz (THz) regimes. Picosecond pulse radiation can be used in broadband spectroscopy, 3-D imaging, and high-speed wireless communication [1]–[4]. In contrast with a bandwidth (BW)-limited continuous-wave radiating source, a picosecond impulse radiator provides broadband spectral information across millimeter-wave and THz frequencies, which can be used to produce hyperspectral images. In addition, ultra-short impulse-radiating arrays with pulse widths of a few picoseconds, and amplitude modulation capability, can be time-interleaved to build Tbit/sec wireless links [5], [6].

Manuscript received January 19, 2017; revised April 18, 2017 and July 12, 2017; accepted August 7, 2017. Date of publication August 30, 2017; date of current version October 23, 2017. This paper was approved by Associate Editor H. Hashemi. This work was supported in part by NSF Career Award, in part by Keck Foundation, and in part by DARPA YFA. (*Corresponding author: M. Mahdi Assefzadeh*.)

The authors are with the Department of Electrical and Computer Engineering, Rice University, Houston, TX 77005 USA (e-mail: mahdi@rice.edu).

Color versions of one or more of the figures in this paper are available online at <http://ieeexplore.ieee.org>.

Digital Object Identifier 10.1109/JSSC.2017.2739180

Traditionally, two different techniques have been used to produce ultra-short pulses in the THz regime. The first technique is based on the excitation of a III–V photoconductive antenna (PCA) with a femtosecond laser pulse [7]–[10], while the second one relies on an oscillator followed by a fast switch to turn on/off the oscillating signal and produce a pulse [3], [4], [11]. In this section, we will review various methods and explain their limitations and advantages.

### A. Picosecond Pulse Radiation Based on a PCA Excited by a Femtosecond Laser

In the PCA-based systems, an optical pulse pump from a femtosecond laser abruptly increases the carrier concentration at the center of a PCA. In the emission mode, a dc bias is applied to the PCA, and when the optical pulse arrives, the photoconductive switch shorts the PCA and generates a fast current with a picosecond rise time. This current drives the antenna and produces THz waves. A similar principle is used to detect THz pulses. In this case, no dc bias is applied to the PCA; instead, a femtosecond laser shorts the junction of the PCA antenna and generates a dc current proportional to the THz field incident on the antenna. To capture the entire waveform, a sub-sampling scheme is deployed, wherein delaying the laser pulse and shifting the sampling window repeat the measurement. This pulse generation and detection technique is widely used in THz time-domain spectroscopy (THz-TDS).

THz-TDS has numerous applications in imaging and spectroscopy. In medical imaging, it has been used for skin cancer detection through measuring the dielectric constant in THz frequencies using it to differentiate between the normal and cancerous cells [12], [13]. THz-TDS has also been used for pharmaceutical applications [14], [15], non-destructive evaluation of materials [16]–[18], explosive detection [19], [20], and security imaging [21].

Although THz-TDS is a powerful technique, it has several limitations. First, it requires a femtosecond laser, which is not only bulky and expensive but also has a low repetition rate (<100 MHz) that limits the average-radiated power. Second, to produce an image, the object must be mechanically scanned, which significantly reduces the acquisition time. Finally, to capture the entire waveform, a sub-sampling scheme is employed, wherein a mechanical delay line is used to shift the laser pulse; this greatly decreases the measurement speed. These limitations render THz-TDS systems rather inaccessible.

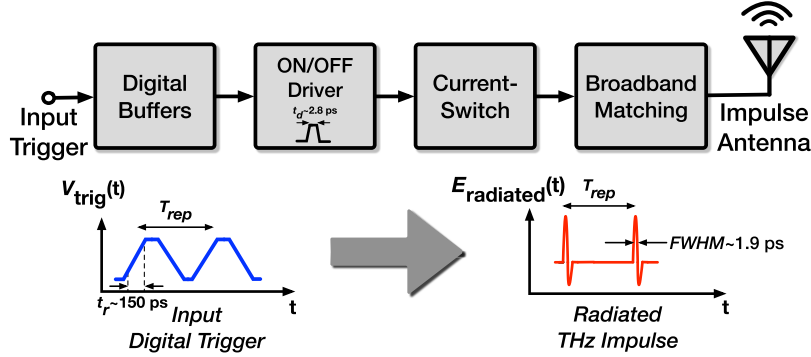


Fig. 1. Block diagram of the D2I architecture.

### B. Oscillator and Switch-Based Pulse Radiation

Conventional architectures of pulse radiators in silicon are based on an on-chip oscillator followed by a fast switch [4]. There are several limitations associated with these methods: first, they suffer from random phase variation of the free-running carrier signal and therefore require a power- and area-consuming phase-locked loop (PLL) [11]. Second, the BW of the generated pulse is limited due to the transient response of the switch. Third, the low isolation of the switch at THz frequencies dramatically degrades the performance and dynamic range of the systems in radar applications. Fourth, since a pulse-radiating system is intended to generate short pulses, the oscillator and the PLL are required to run continuously and cannot be turned off fast. This limitation results in a high-power consumption. Finally, area-consuming PLLs and delay-locked loops limit the scalability of these transmitters. In this paper, a novel oscillator-free solution is proposed and successfully implemented in silicon, overcoming the aforementioned limitations.

## II. DIRECT DIGITAL-TO-IMPULSE RADIATION: OSCILLATOR-FREE SIGNAL GENERATION

Direct digital-to-impulse (D2I) signal generation is inspired by the spark gap transmitter, which was invented in the beginning of the twentieth century. This transmitter radiated pulsed electromagnetic waves by generating a fast flow of current through a spark gap and coupling it to an antenna [22].

Unlike current signal generation methods in the millimeter-wave and THz regimes, D2I signal generation does not rely on an oscillator. Instead, an ultra-sharp, high-amplitude rising or falling edge of electrical current is generated by a fast current-switch and delivered to a broadband, phase-linear impulse antenna. The antenna is designed to act as an inductor in low frequencies (short circuit in dc), generating a large voltage impulse when the current is switched ON/OFF. An input digital trigger is fed to the chip to synchronize the generated impulse and control the starting time of the radiation [23]–[25].

The impulse radiation mechanism can be explained according to two modes of operation. In one mode, a dc current is initially stored in the impulse antenna. By opening the switch,

this current is interrupted, converting the stored magnetic energy to a radiated impulse in the THz regime. Similarly, the second mode of operation starts with zero initial current and an impulse signal is radiated, when the current is turned on. Therefore, a positive or negative impulse can be generated by a fast rising or falling change in the current of the antenna, respectively. Both these modes of operation can be used to generate impulses. However, due to a spurious narrowband resonance produced by the combined network of the antenna, parasitic capacitors, and bond wires, a ringing follows the radiated impulse. This narrowband resonance occurs at a much lower frequency and has a smaller BW than the actual impulse. An ON/OFF impulse-shaping technique is designed and implemented to suppress this low-frequency ringing. In addition, two capacitor arrays are used to de-Q and suppress this oscillation and to maximize the amplitude of the radiated impulse by canceling the effects of parasitic inductors and bond wires. In Section III, we will discuss these methods in detail.

Fig. 1 shows a system-level block diagram of D2I. As shown later in this section, an on-chip impulse antenna is designed and its near- and far-field circuit models are derived. These models are used in the design process in both the frequency- and time-domain simulations. In Section III, the design of the circuit is described in detail.

### A. On-Chip Impulse Antenna

In order to achieve a large BW, high efficiency, and low-cost solution, a D2I radiator is required to employ an on-chip antenna. An integrated antenna provides a large BW by eliminating lossy and narrowband connections (such as bond wire) between the chip and an off-chip antenna. It also reduces the cost of assembly by eliminating the need for precise alignment of the off-chip antenna. In this paper, an on-chip slot bowtie antenna is designed and successfully tested. In addition to the antenna impedance, its near- and far-field responses are carefully simulated.

One of the key challenges in designing an efficient broadband on-chip antenna is the undesired effects of substrate modes, which make the antenna narrowband, reduce its efficiency, and cause ringing. They also introduce substantial non-linearity in the phase response of the antenna. To avoid these

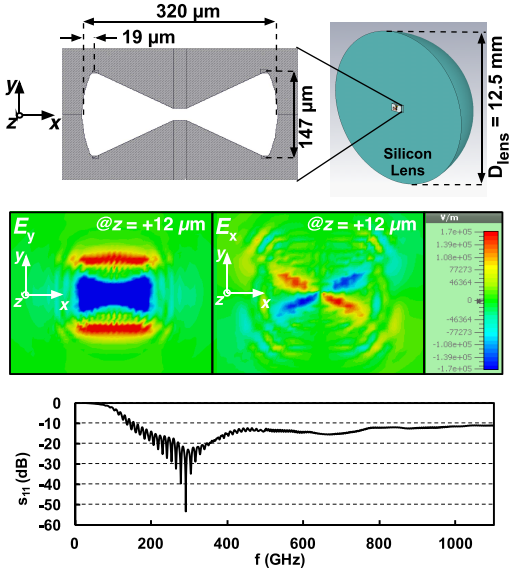


Fig. 2. Antenna setup, simulated near-field  $E$ -field, and  $S_{11}$  of the antenna.

undesired effects caused by a planar substrate, a hemispherical high-resistivity silicon lens is attached under the chip to mimic a semi-infinite silicon substrate for the antenna. The silicon lens increases the radiation efficiency and maximizes the BW by eliminating the substrate modes [26], [27].

The antenna used in the D2I design must have a broadband impulse response with a linear phase to radiate an ultra-short pulse. In addition, the D2I topology requires an antenna that behaves like an inductor in low frequencies. To address these challenges, a slot bow-tie antenna is designed and optimized by adjusting its dimensions. In addition, the edges of the antenna are curved to enhance its BW [28], [29]. Fig. 2 shows the geometry of the antenna, which is fabricated using an on-chip copper metal layer (M5) with a thickness of 1.5  $\mu\text{m}$ . The antenna radiates to the substrate of the silicon chip, which is mounted on back of a high-resistivity silicon lens. The thickness of the silicon substrate is 200  $\mu\text{m}$ , while its resistivity is  $10 \Omega \cdot \text{cm}$ . The silicon lens has a hemispherical shape with a diameter of 12.5 mm, an extension length of 300  $\mu\text{m}$ , and resistivity of  $10 \text{k}\Omega \cdot \text{cm}$ .

Two-shielded microstrip transmission lines are used as a differential pair to feed the circulating current through the antenna. The near field of the antenna is simulated to find a suitable position for the shielded microstrip feed structure. Electric fields in  $x$ - and  $y$ -directions at 12  $\mu\text{m}$  above the antenna plane are shown in Fig. 2. As shown in Fig. 2, to minimize the impact of the transmission lines on the radiation pattern, they are placed along the  $x$ -direction at the center of the antenna, where  $E_x$  is zero. The width of the horizontal feeds is minimized to reduce the effect on  $E_y$ . In addition, the circuit components are placed far from the sharp corners of the antenna, where the  $E$ -field is large. The  $S_{11}$  of the whole structure including the antenna, silicon substrate, and lens is simulated and plotted in Fig. 2.

Fig. 3 shows the directivity (at  $\theta = 180^\circ$ ) and radiation efficiency of the slot bow-tie antenna. These parameters are

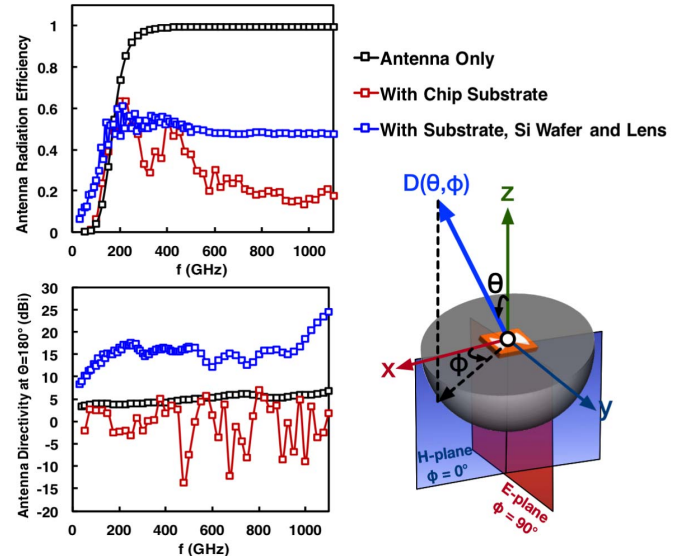


Fig. 3. Simulated radiation efficiency and directivity at  $\theta = 180^\circ$  for different scenarios.

plotted in three scenarios: antenna only (in free space), antenna with chip substrate, and antenna on-chip substrate with silicon wafer and lens underneath. The fluctuations in the directivity and radiation efficiency of the case with silicon lens are caused by internal reflections inside the silicon lens and the chip substrate. To avoid these reflections, the outer surface of the silicon lens can be coated with a quarter-wavelength matching layer but this will reduce the BW [30]–[34].

#### B. Broadband Near- and Far-Field Antenna Models

The slot bow-tie antenna can be modeled as a single-input, double-output system, wherein its input is the current of the antenna port. The first output is the near field of the antenna, while the other output is the far-field radiation. The induced voltage on the antenna is affected by its near field, which has a different response than the far field. The near-field response directly affects the switching performance of the active core circuit and also, in the case of an array, impacts the nearby radiating elements. Since the ultimate goal is to radiate short pulses, the design is optimized to minimize the duration of the radiated signal in the far field.

The near- and far-field impulse responses of the antenna in the time and frequency domains are simulated and shown in Fig. 4. In this simulation, the 3-dB BW of the input excitation (a current impulse fed to the antenna) is 400 GHz. By comparing the magnitude and group delay variation of the impulse responses, it is observed that the far-field response has a much larger BW. In addition, the strong ringing on the antenna voltage is mostly due to the non-radiative near field. As will be discussed in detail in Section III, this ringing is canceled using a novel ON/OFF impulse-shaping technique.

In this paper, the estimated linear time-invariant (LTI) transfer functions of the antenna in the near and far fields are synthesized and used in circuit simulations. The key idea is to synthesize Laplace-domain transfer functions for both

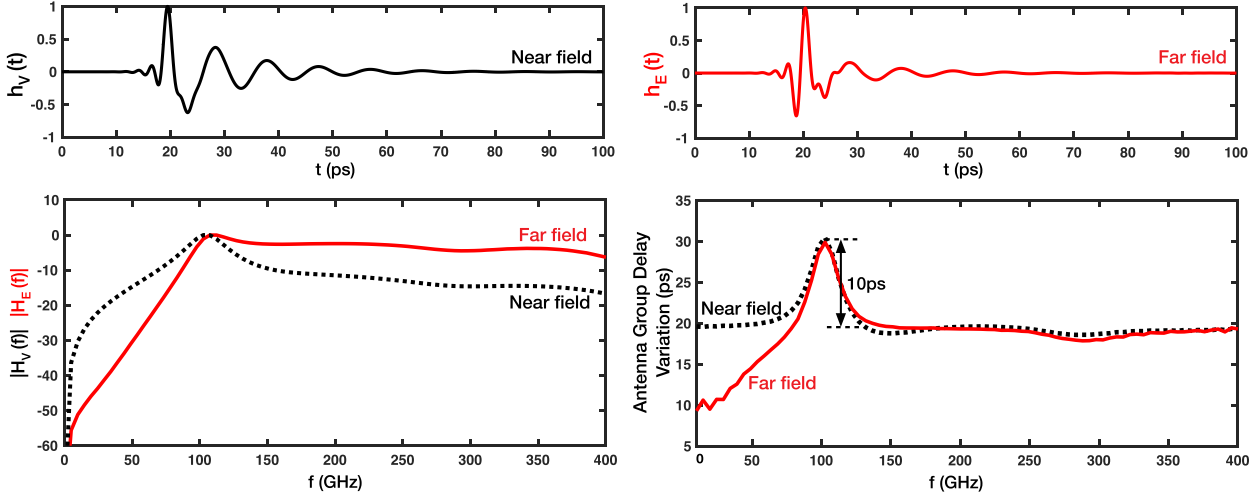


Fig. 4. Simulated antenna voltage and far-field  $E$ -field in time and frequency domains in response to an impulse current input with a 3-dB BW of 400 GHz.

the lumped and the far-field antenna models. The following paragraphs describe how the transfer functions are synthesized: First, an impulse current is fed to the antenna in an EM solver CST Microwave Studio. This simulation is used to acquire the impulse responses of the antenna voltage (the near-field effect) and far-field  $E$ -field. The acquired impulse responses are used with the transfer function toolbox provided by Mathworks MATLAB (function “tf”) to create LTI systems that fit the results of the EM simulation. The order of these systems (number of poles), in addition to causality and stability check of the created systems are controlled. The near-field model is estimated as a second-order RLC circuit, while the far field is modeled as a fourth-order transfer function transformed into an  $s$ -domain (Laplace-domain) current-controlled voltage source (SCCVS) in a Cadence Spectre simulator (Fig. 5). The zeros and poles of these two transfer functions are extracted and shown in Fig. 6. This method provides significant benefits in attaining simulation convergence and reduced runtime in transient simulations, compared to a simple S-Parameter block in cadence. A comparison between the synthesized models (lumped and far-field models of the antenna) and the EM simulation results in the frequency domain is shown in Fig. 6.

### C. Tunable Frequency-Comb Generation and Radiation

In D2I, the strongly nonlinear current-switching mechanism results in the generation of numerous harmonics of the trigger signal, ranging from gigahertz to THz. Having a high-power, broadband frequency-comb source is crucial in many applications such as hyper-spectral imaging and wideband spectroscopy. By feeding a periodic trigger signal to a D2I radiator, an impulse train is radiated in the time domain with a repetition rate set by the frequency of the input trigger signal. Assuming  $x_1(t)$  to be a single-radiated impulse signal, the time-domain impulse train  $x(t)$  can be written as

$$x(t) = x_1(t) * \sum_{k=-\infty}^{\infty} \delta(t - kT) = \sum_{k=-\infty}^{\infty} x_1(t - kT) \quad (1)$$

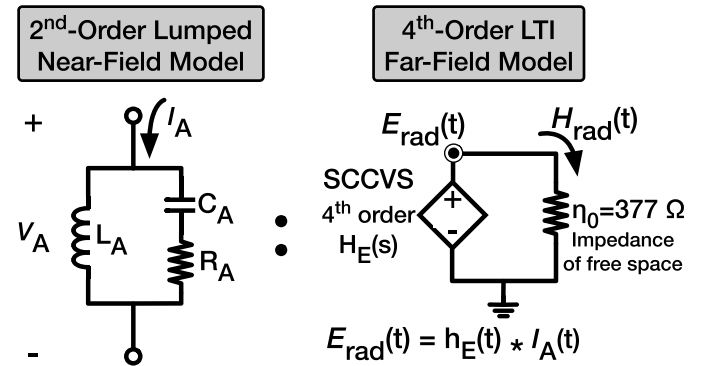


Fig. 5. Near- and far-field models of the antenna used in transient circuit simulations. The time-domain radiated  $E$ -field is acquired by the convolution between  $h_E(t)$  (far-field impulse response of the antenna) and  $I_A(t)$  (antenna current).

where  $T$  is the period of the impulse train. The Fourier transform of  $x(t)$  is

$$X(f) = \frac{1}{T} X_1(f) \sum_{k=-\infty}^{\infty} \delta\left(f - k \frac{1}{T}\right) \quad (2)$$

in which  $X_1(f)$  is the Fourier transform of a single impulse signal. Thus, the frequency spectrum of an impulse train is a sampled version of the frequency spectrum of a single impulse with steps of  $1/T$ . To perform spectroscopy,  $T$  can be tuned to sweep the entire spectrum.

There are some pros and cons associated with larger or smaller trigger frequencies. Low trigger rates lead to the radiation of a frequency comb with smaller frequency steps (Fig. 24), which provides spectral information in a large number of harmonic frequencies. However, although large trigger frequencies provide a lower number of tones across the THz spectrum, they provide stronger tones suitable for spectroscopy at a certain frequency. For example, using (2), it is shown that increasing the repetition rate by a factor of ten results in the generation of frequency tones that are 20 dB larger in power at the original frequencies. It is worthy of

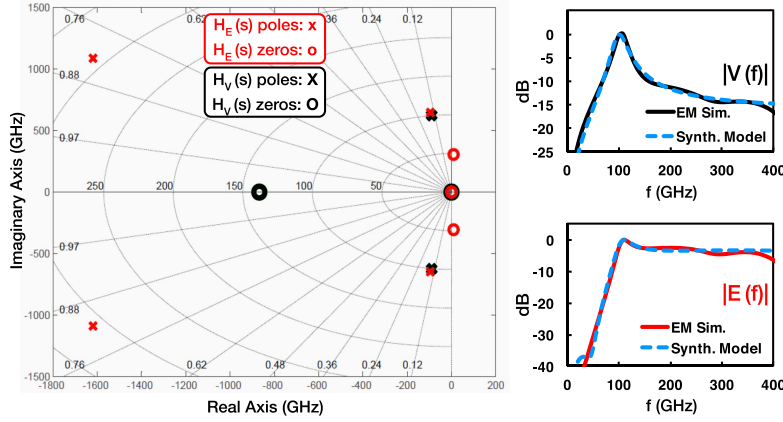


Fig. 6. Pole-zero plots of near- and far-field antenna models and comparison of the EM simulation results to the synthesized models.

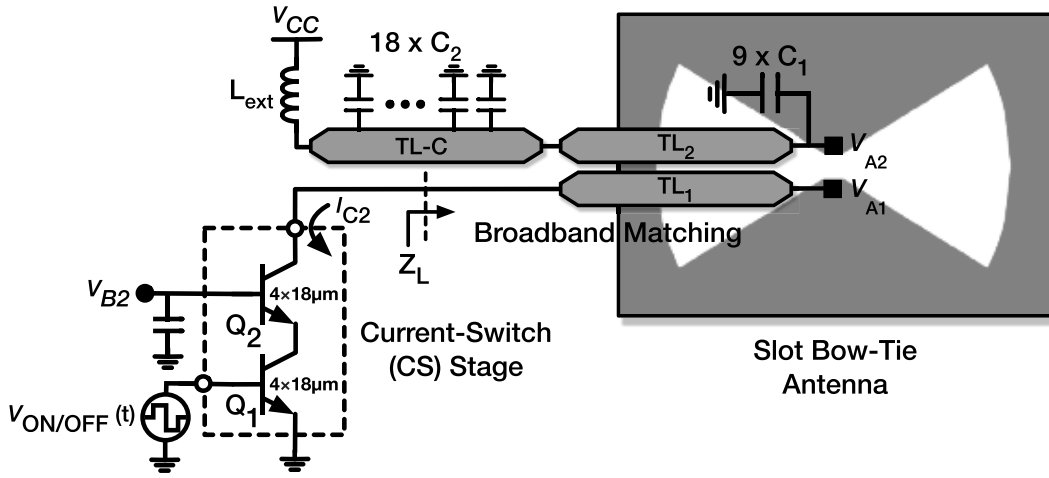


Fig. 7. Circuit schematic of the current-switch stage.

note to mention that, in both cases, any selected tone can be fine-tuned by changing the trigger rate.

### III. CORE SWITCHING CIRCUIT

#### A. Current Switch

A high-speed current switch is required to turn the antenna current ON and OFF with a short rise/fall time of a few picoseconds. A cascode bipolar switch is used to rapidly switch the circulating current of the antenna. A cascode topology is favored over a single bipolar transistor for the following reasons: first, a cascode switch minimizes the loading effect on the previous stage by avoiding the Miller effect, and second, the output resistance of a cascode is larger than a single transistor, which increases the amplitude of the radiated impulse. The larger output resistance of a cascode, with respect to a single transistor, relaxes the requirement for output matching at high frequencies. This results in a higher matching efficiency (Fig. 10). As shown in Fig. 9, the load impedance of the cascode current switch  $Z_L$  has a resistance of around  $10\Omega$  at 160 GHz. However, if only a single transistor was used, simulation shows the output resistance at 160 GHz would drop to  $6\Omega$ . The higher output resistance of cascode relaxes the requirement for impedance matching and minimizes the

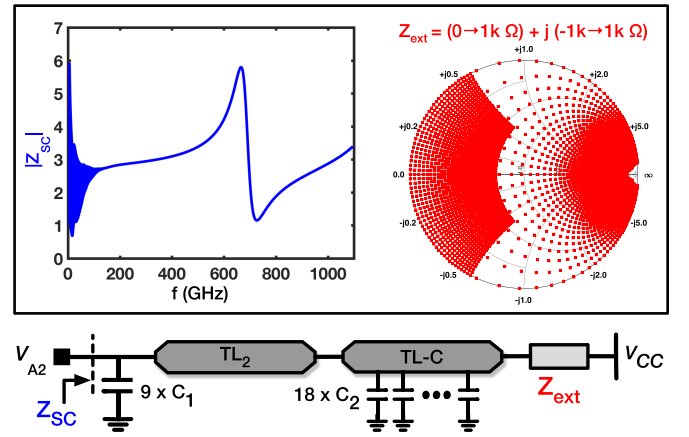


Fig. 8. Broadband ac short circuit that provides fast charge injection at the time of switching. Simulation is performed while the external impedance by the pad is swept across complex but passive impedances.

loading effect on the previous stage by avoiding the Miller effect.

1) *Broadband AC Ground at Antenna Supply Node ( $V_{A2}$ ):* Fig. 7 shows the circuit schematics of the current-switch stage

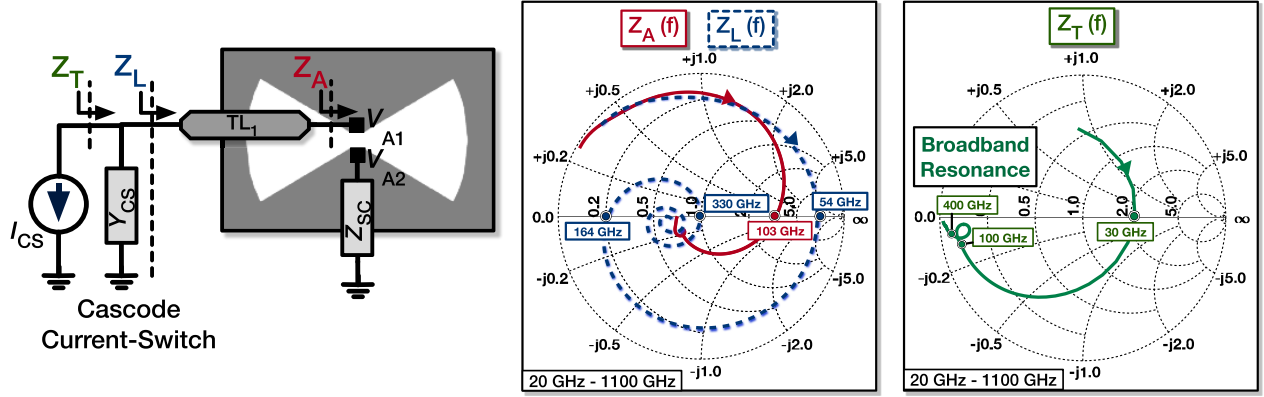


Fig. 9. Smith charts of the simulated antenna impedance, the load impedance, and the total output impedance of the current switch, plotted in frequency. A broadband resonance is observed in the total impedance.

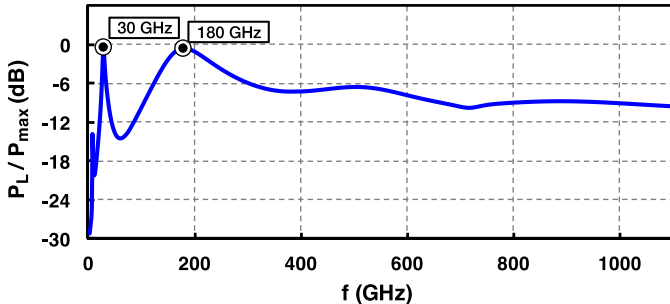


Fig. 10. Simulated power transfer ratio from the current switch to the antenna, calculated based on the delivered power divided by the maximum available power in conjugate-matched condition. A ratio of one represents a perfect conjugate-matched condition.

connected to a slot bow-tie antenna with shielded microstrip feedlines. To cancel the inductive effects of the bond wire and the upper feed line ( $TL_2$ ), which reduce the speed of the current switching; a broadband short circuit is needed at node  $V_{A2}$ . To achieve this broadband response, different values of MIM capacitors with different SRFs are required. In this paper, due to the limited chip area, two sets of capacitors are used. The first set consists of nine 500-fF capacitors ( $C_1$ ) that are placed at node  $V_{A2}$ . Each of these capacitors has an SRF of 80 GHz and their capacitive role is aimed at lower frequencies. The impedance above the SRF is still below  $18 \Omega$  up to 400 GHz. The estimated imaginary part of the impedance of each of 500-fF capacitors is  $52 \Omega$  at 1.1 THz (the real part is negligible). To achieve a short circuit at millimeter-wave and THz frequencies and to provide fast current injection at the time of switching, a transmission line-capacitor ladder network is designed that includes  $18 \times 80$ -fF capacitors, each having an SRF of 240 GHz. The estimated imaginary part of the impedance of each 80-fF capacitor is  $54 \Omega$  at 1.1 THz.

To evaluate the broadband ac short circuit, the impedance seen by the antenna at node  $V_{A2}$ ,  $Z_{SC}$ , is simulated while the external impedance of packaging seen from the pad  $Z_{ext}$  is swept across a large range of complex but passive impedances. The real part of  $Z_{ext}$  is changed from  $0 \Omega$  to  $1 \text{ k}\Omega$  while the imaginary part of  $Z_{ext}$  is swept between  $-1$  and  $1 \text{ k}\Omega$ , for frequencies up to 1.1 THz. A total number of 33 000 simulations

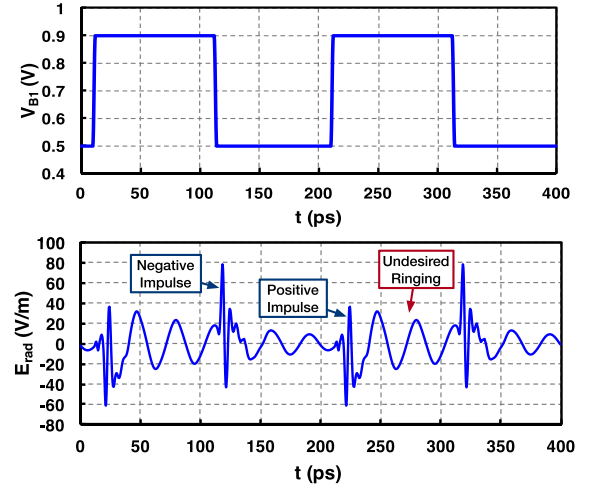


Fig. 11. Simulated response of the radiated  $E$ -field to a voltage-step at the input of the current-switch stage at the base of transistor  $Q_1$  ( $V_{B1}$ ).

are performed to cover a large number of different external impedances that could be seen by the pad at different frequencies. To be able to perform a large number of simulations with a decreased overall simulation runtime, a two-port S-Parameter box is generated using the bypassing network (Fig. 8) and imported in a MATLAB program to numerically calculate  $Z_{SC}$  while  $Z_{ext}$  is changed. For each simulation,  $Z_{ext}$  is considered to be complex but passive impedance that is frequency-independent. The change in the imaginary part of  $Z_{ext}$  is specifically important to track undesired resonances that could result in a large  $Z_{SC}$  value seen at node  $V_{A2}$ . Consequently, the absolute value of the resulting short-circuit impedances are shown in Fig. 8 to provide an illustration of the higher limits of  $Z_{SC}$  at each frequency.

**2) Broadband Output Matching of the Current Switch:** A shielded microstrip line ( $TL_1$  in Fig. 9) is designed to carry the circulating current to the antenna at node  $V_{A1}$ . Although the antenna has a single dominant resonance at 103 GHz, the impedance seen at the input of the feed line ( $Z_L$ ) shows more resonance frequencies due to the impedance transformation effect of the transmission line. Fig. 9 shows this

impedance on a Smith chart and compares it to the antenna impedance ( $Z_A$ ).

The total load impedance of the current-switch stage (including its own output resistance and parasitic capacitance) is also shown in Fig. 9. This plot shows a narrowband resonance at 30 GHz and a broadband resonance around 180 GHz. This frequency, which is the center frequency of the resonance, can be tuned by varying the length and characteristic impedance of the feed transmission line. In addition,  $Z_L$  is varied to provide wideband conjugate matching. The power transfer ratio,  $P_L/P_{\max}$  (in which  $P_L$  is the power delivered to the load and  $P_{\max}$  is the maximum available power in the conjugate-matched condition), is shown in Fig. 10. As shown in Fig. 10, apart from the 180-GHz matched resonance, a low-frequency peak is present, which is an undesired, narrowband effect caused by the first resonance of the combined network of the parasitic output capacitor of the cascode switch and the first-order inductance of the transmission line and antenna. As will be described later in this section, this low-frequency narrowband effect will be suppressed using an ON/OFF impulse-shaping technique.

*3) Response of the Radiated Field to a Voltage Step at the Input of the Current Switch:* Transient simulations of the radiated far-field  $E$ -field, in response to a positive and negative voltage-step input to the base of transistor  $Q_1$ , are shown in Fig. 11. The responses are plotted for a rise and fall time of 1 ps at the input. This plot shows that a 30-GHz ringing after the main pulse. This ringing is stronger in the near field (antenna voltage). This effect is smaller in the far field because the antenna's radiation efficiency is smaller at 30 GHz (<10%). However, this undesired effect can be critical in many applications. For instance, in short-distance pulsed radar transceivers, the signal from the transmitter needs to be completely turned off to avoid saturating the receiver.

To optimize the radiated impulse, two design goals must be achieved. First, the peak amplitude and BW (minimizing pulse width) of the radiated impulse should be maximized. This is achieved using a broadband resonance and matching network explained earlier in this section. Second, the 30-GHz undesired narrowband resonance should be suppressed. In the following section, we introduce an ON/OFF impulse-shaping technique to achieve the second goal.

### B. ON/OFF Impulse-Shaping Technique

To cancel the ringing produced by the narrowband resonance at 30 GHz, an ON/OFF impulse-shaping technique is designed and implemented. First, a positive (rising) current edge is turned on and fed through the load of the current switch. As shown in the previous section, this rising current edge generates two signals: a broadband impulse and a 30-GHz undesired ringing (Fig. 11). Subsequently, after a tunable picosecond-scale time delay ( $t_d$ ), a negative current edge is fed to the load by simply turning off the current switch. The latter event suppresses the 30-GHz ringing by adding two out-of-phase transient oscillations. Meanwhile,  $t_d$  is tuned to add up the two generated broadband impulses constructively. Fig. 12 shows the simulation results of the radiated signal after applying this technique for different

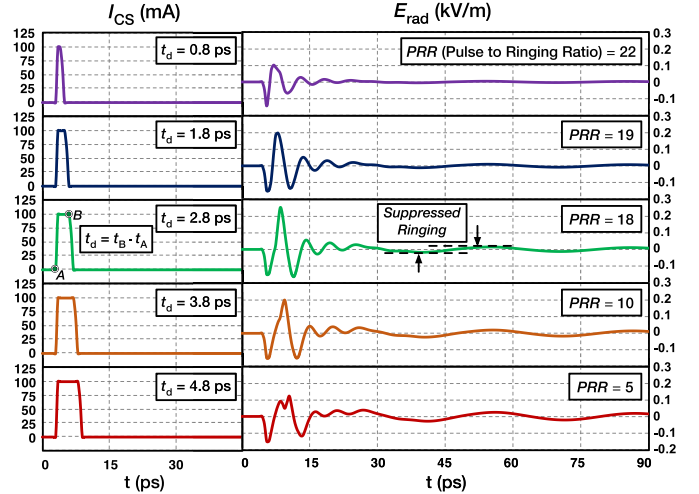


Fig. 12. Simulation results of the radiated signal after applying the ON/OFF impulse-shaping technique for different values of  $t_d$ .

$t_d$  values. Fig. 12 shows how different waveforms at node  $V_{B1}$  affect the radiated  $E$ -field. In this design,  $V_{B1}$  charges the base node of a bipolar transistor. When the base is charged, the effective collector-emitter resistance of the transistor is reduced, which allows the current to pass the transistor. When  $V_{B1}$  is reduced, the charge stored at the base node of the bipolar transistor is removed. At the end of this process, the collector-emitter resistance of the bipolar transistor increases rapidly, which stops the current of the transistor. This disruption in current, results in a rapid change in the current of the antenna, which triggers a high-frequency radiation.

In order to quantify this ringing-canceling effect and the limitations imposed by this technique on the BW and phase linearity of the radiated impulse, the described ON/OFF method is expressed as an LTI transfer function that converts the signal generated by a single positive current step to a short pulse with minimal ringing. The resulting frequency-domain transfer function ( $H_{10}$ ), its magnitude, and group delay ( $\tau_{g10}$ ) can be expressed in the following explicit terms:

$$H_{10}(\omega, t_d) = 1 - e^{-j\omega t_d} \quad (3)$$

$$|H_{10}(\omega, t_d)| = 2 \left| \sin \frac{\omega t_d}{2} \right| \quad (4)$$

$$\tau_{g10}(\omega, t_d) = -\frac{\partial}{\partial \omega} (\angle H(\omega, t_d)) = \frac{t_d}{2}. \quad (5)$$

It is shown by (4) that the peak of  $|H_{10}(\omega)|$  can be tuned at 180 GHz by choosing a  $t_d$  of 2.8 ps. Based on this time delay, the amplitude of the 30-GHz ringing will be attenuated by 52%, while the 180-GHz impulse amplitude will be doubled; therefore, the ringing amplitude will be relatively attenuated by 76%. In other words, the ratio of impulse peak amplitude to spurious ringing (180 to 30 GHz, respectively) will be 4.2 times larger than that of the case without the ON/OFF technique. The fractional 3-dB BW of  $|H_{10}(\omega)|$ , with reference to its peak centered at 180 GHz, is 100%; meanwhile, the fractional 3-dB BW of the ON/OFF technique, with reference to its input signal (single impulse in response to a positive current step), is 158%. In addition, this technique has

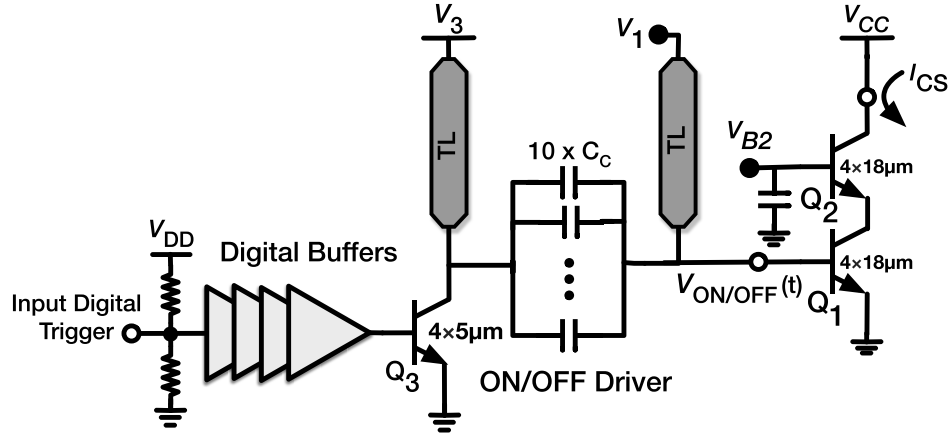


Fig. 13. Circuit schematic of the ON/OFF driver.

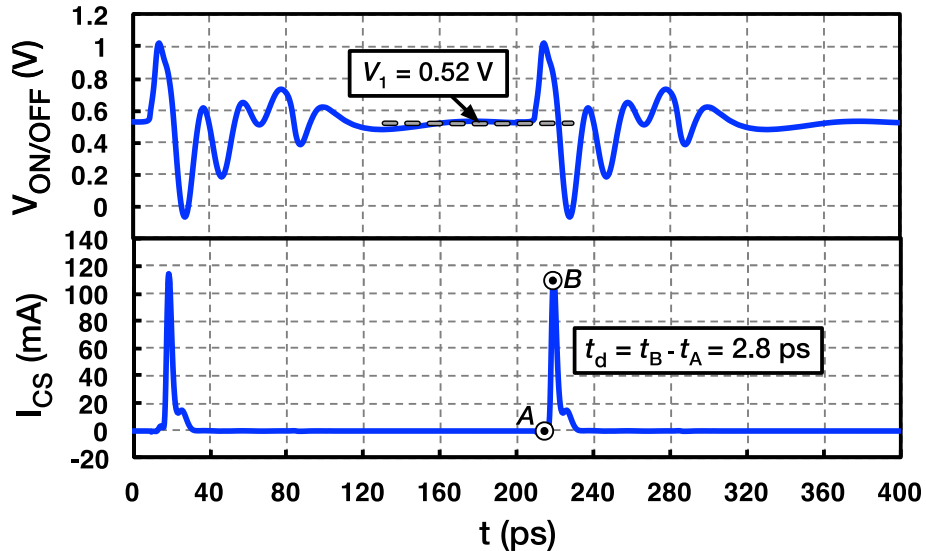


Fig. 14. Simulated ON/OFF driving voltage and the generated current from current switch with a  $t_d$  of 2.8 ps.

a phase-linear response with a constant group delay of 1.4 ps. Therefore, the ON/OFF technique does not disperse the impulse signal.

*1) ON/OFF Driver:* To implement the ON/OFF impulse-shaping technique at the circuit level, a sharp rising and falling voltage edge must be generated and fed to the base of the current switch. To achieve this, an intermediate ON/OFF driving amplifier is designed that employs inductive peaking to generate a sharp voltage. The circuit schematic of this amplifier and the preceding inverters used as buffers is shown in Fig. 13. Transistor  $Q_3$  in the driving amplifier generates an ON/OFF signal by switching the current of its inductive load. This process results in a voltage spike at the output of the driving amplifier. The input of the driving amplifier is provided by a series of NOT stages, which reduce the rise/fall time of an external digital trigger. Four inverters reduce the rise and fall time of the input trigger from 150 to 30 ps. Fig. 14 shows the ON/OFF driver signal, which features a 3.4-ps rising and 4.5-ps falling edges (0.8–1 V). The simulated current pulse generated by the current switch is shown in Fig. 14, showing a

peak current of 115 mA and a rise/fall time (10%–90%) of 1.8 ps/2.4 ps, respectively. The time delay between the rising and falling edges of the current in this technique  $t_d$  is tuned to 2.8 ps by setting the bias voltage  $V_1$  to 0.52 V.

### C. Final Simulation Results and DC-to-Radiated Efficiency

Fig. 15 shows the schematic of the output stage. The final simulation results of the radiated  $E$ -field in the time and frequency domains are shown in Figs. 16 and 17. A 5-GHz repetition rate is used for the trigger, with the resulting radiated signal having a full width at half maximum (FWHM) of 1.9 ps, a central frequency of 160 GHz, and a 3-dB BW of 130 GHz (10-dB BW of 200 GHz). The simulation results show a peak pulse-radiated power of 3.2 mW and a peak pulse effective isotropic-radiated power (EIRP) of 20.3 dBm. The peak pulse EIRP is calculated using the following equation:

$$\text{EIRP}_{\text{peak}} = \frac{|\mathbf{E}_{\text{rad}}|_{\text{peak}}^2}{\eta_0} (4\pi R^2) \quad (6)$$

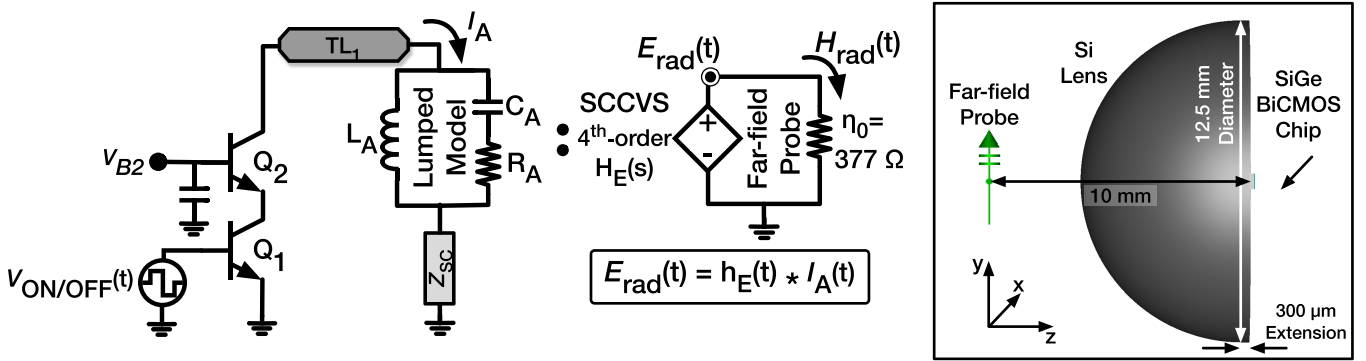


Fig. 15. Circuit schematic of the output stage and a detailed illustration of the near- and far-field models used for final simulations.

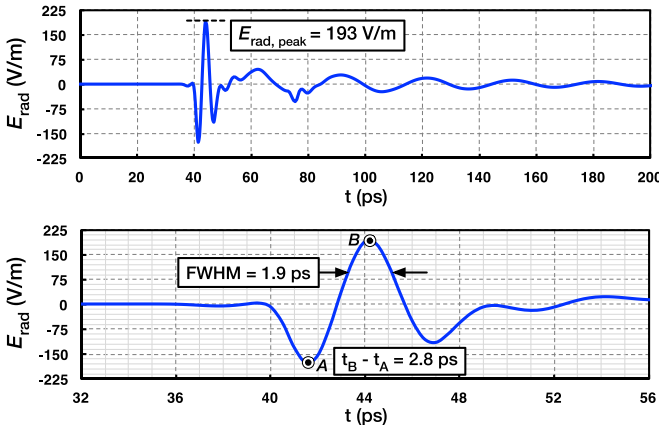


Fig. 16. Simulated radiated \$E\$-field probed at a distance of 1 cm showing a peak value of 193 V/m and an FWHM of 1.9 ps.

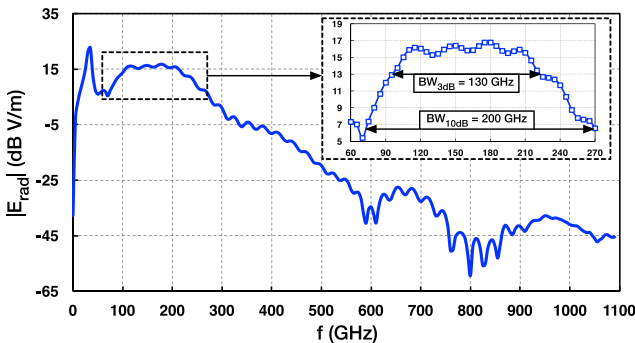


Fig. 17. Simulated frequency spectrum of the radiated \$E\$-field.

where \$R = 1 \text{ cm}\$ is the distance of the \$E\$-field probe from the antenna, \$|E\_{rad}|\_{peak}\$ is the peak of the radiated \$E\$-field in time, and \$\eta\_0 = 377 \Omega\$ is the wave impedance of free space.

The ON/OFF technique significantly increases the dc-to-radiated efficiency of the current switch by turning the switch completely OFF shortly after the impulse is radiated. The output current-switch stage consumes 1.44 pJ in a 200-ps period (7.2-mW average power), while the energy

of the radiated impulse is 32 fJ. This results in a 2.2% dc-to-radiated efficiency of the current-switch stage, which includes the radiation efficiency of the antenna. The dc-to-radiated efficiency of the entire circuit is 0.33%, which is calculated based on the energy of the radiated impulse (32 fJ) divided by the dc energy consumed by the entire circuit in a single repetition period (9.8 pJ).

#### IV. CHIP CHARACTERIZATION IN BOTH TIME AND FREQUENCY DOMAINS

##### A. Time-Domain Characterization With a Femtosecond-Laser-Based THz-TDS System

One of the main challenges of sampling a picosecond pulse in the time domain is ensuring that both the receiver and its antenna are broadband and have a linear phase response. Pyramidal horn antennas cannot be used to receive picosecond pulses, due to their limited BW and nonlinear phase response [35]. In addition, commercially available sampling oscilloscopes have a 3-dB BW of less than 70 GHz, therefore cannot be used to sample a pulse with an FWHM of \$\sim\$2 ps.

To address this, in this paper a custom time-domain measurement system is developed to characterize the time-domain waveform of the radiated pulses using a THz-TDS system equipped with a PCA [25]. An Advantest TAS7500TS femtosecond-laser-based THz sampling system is used to capture the time-domain signal radiated from the chip. On the receiver side, an Advantest TAS1230 PCA samples the THz waveform. The operation of the Advantest THz-TDS system is based on two 50-MHz femtosecond lasers that are locked but have a 5-Hz difference in their repetition rates. This difference in the repetition frequency enables the detector PCA to sample a 20-ns-long THz wave radiated by the emitter PCA in a 200-ms period. Our measurement setup locks our chip to the emitter laser and the detector is used to sample the THz wave radiated by the chip.

The repetition frequency of the impulse-radiating chip is synchronized with the laser using a custom synchronization chain, as shown in Fig. 18. This setup synchronizes a Keysight E8257D signal generator with a 50-MHz electrical signal extracted from the pulsed laser. The 50-MHz electrical signal is conditioned and its frequency is divided by a factor

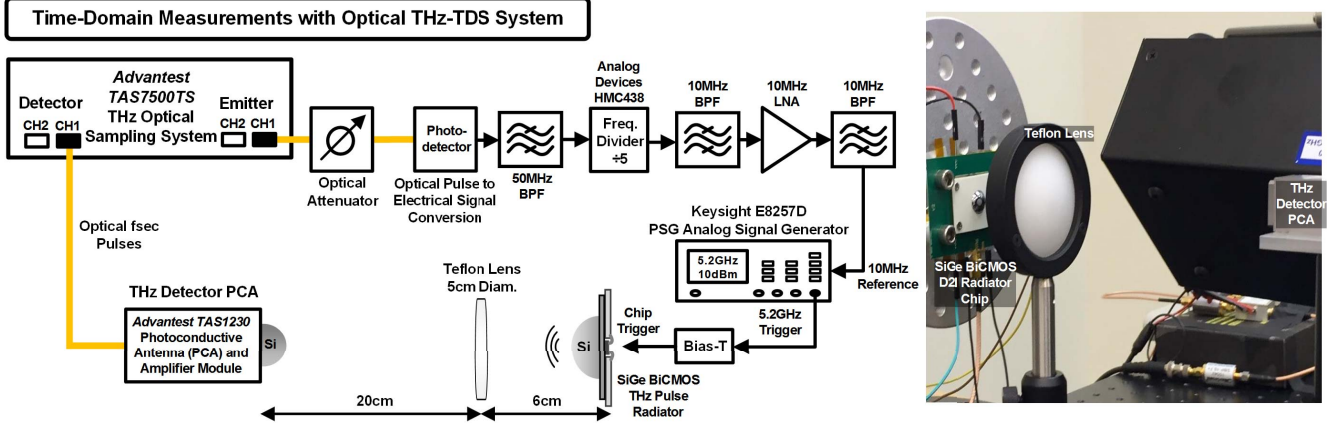


Fig. 18. Time-domain measurement setup developed with a femtosecond-laser-based THz-TDS system.

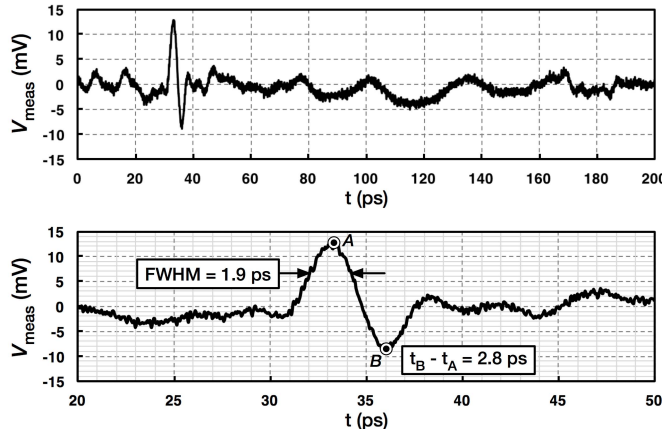


Fig. 19. Time-domain measurement result of the captured THz waveform.

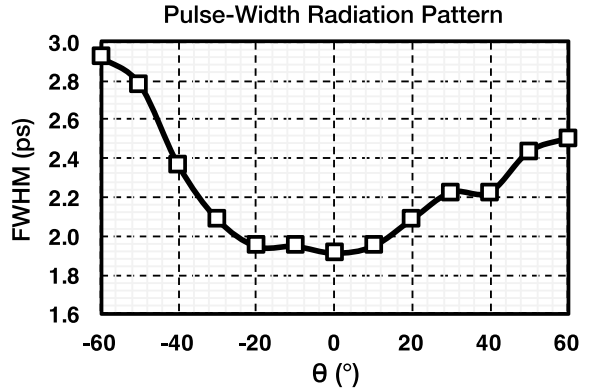


Fig. 21. Measured pulse-width radiation pattern in *E*-plane.

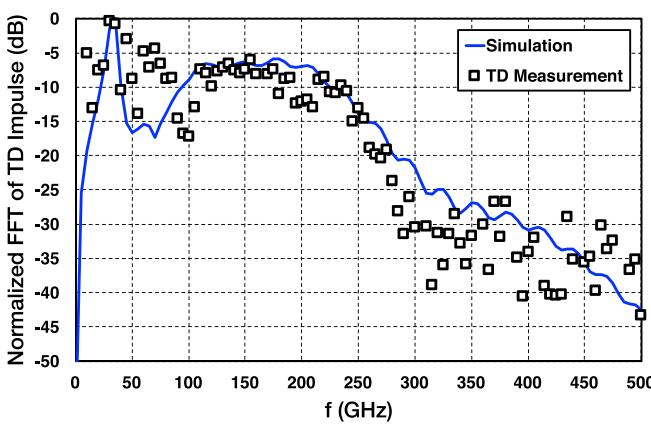


Fig. 20. FFT of the radiated pulse in measurement and simulation.

of five. The resulting 10-MHz reference signal is fed to the 10-MHz reference input of the signal generator. In this paper, a repetition rate of 5 GHz is chosen considering the fact that changing the repetition rate does not change the operation of the impulse radiator. The upper limits on the trigger rate are

the switching speed (rise and fall time) of the digital buffers and the filtering effect of the bond wire.

Fig. 19 shows the measured time-domain waveform of the radiated impulse, which achieves an FWHM of 1.9 ps and a minimum-to-maximum time of 2.8 ps. In this measurement, an averaging number of 512 is used to record the received THz waveform. The single-sided fast Fourier transform (FFT) of the time-domain signal is plotted against the simulation result in Fig. 20. The time-domain *E*-plane pulse-width radiation pattern of the impulse radiator is measured and shown in Fig. 21. Based on this characterization, the FWHM of the radiated impulse changes from 1.9 ps at a 0° elevation angle to 2.8 ps at an angle of 60°, while it is 2.2 ps at 30°.

#### B. 0.05–1.1-THz Frequency-Domain Measurements

The performance of the chip is independently characterized using a frequency-domain measurement setup, as shown in Fig. 22. The mixer port of a Keysight N9030A PXA signal analyzer is used with OML harmonic mixers and horn antennas WR-15, 10, 08, 05, and 03 to cover 0.05–0.325 THz and with VDI SAX Mixers and Horn Antennas WR-2.2, 1.5, and 1 to cover 0.33–1.1 THz. For each of the harmonic mixers, the calibration test data provided by the manufacturer are used to calibrate the received power. The conversion

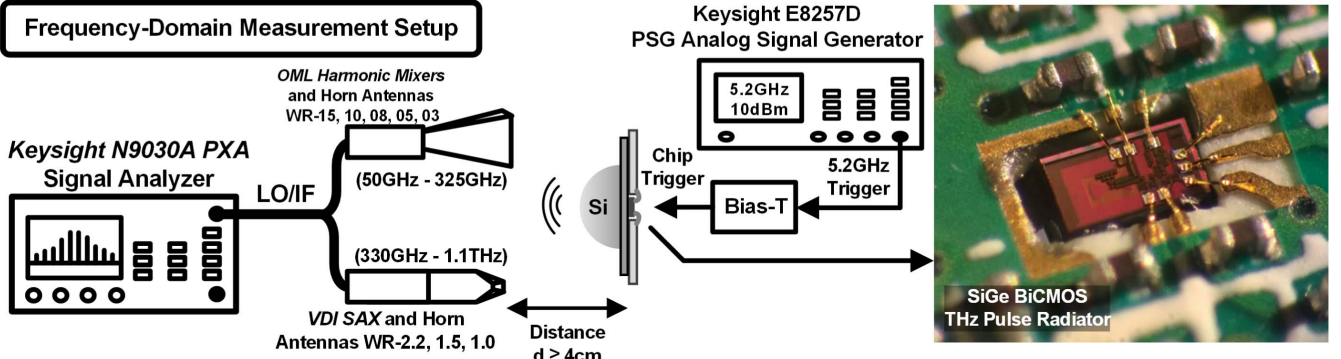


Fig. 22. 0.05–1.1 THz frequency-domain measurement setup.

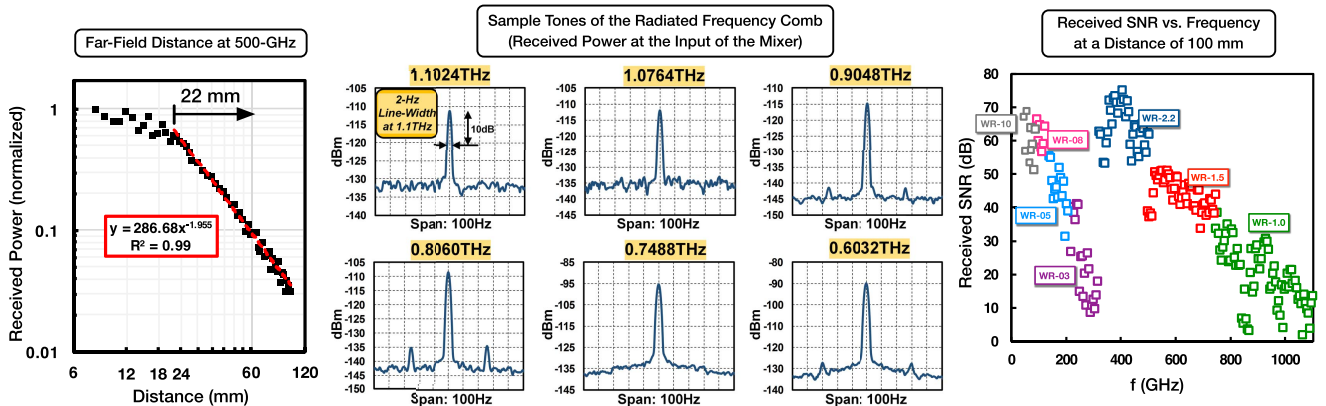


Fig. 23. Far-field distance measurement at 500 GHz, sample measured tones of the radiated frequency comb, and measured received SNR versus frequency.

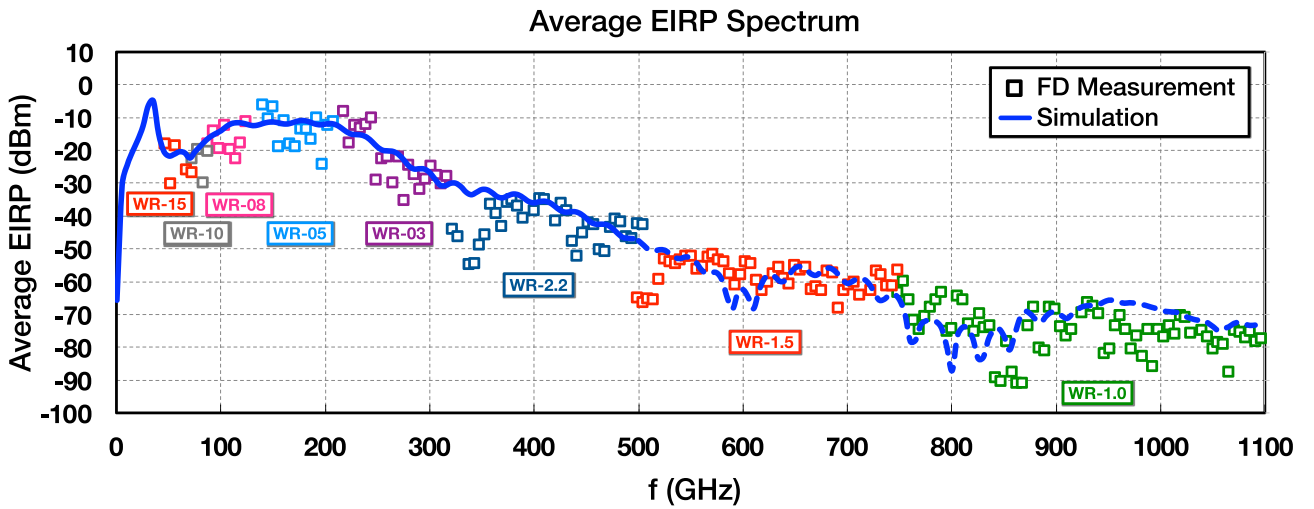


Fig. 24. Average EIRP spectrum measurement results plotted against the simulation results.

loss and the gain of the IF amplifier (for VDI mixers) are de-embedded for each frequency tone. The distance between the chip and the horn antenna is greater than 4 cm in all of the frequency-domain measurements to ensure a far-field operation. A 5.2-GHz trigger signal with 10-dBm power is fed to the 50- $\Omega$  input of the chip through a bias-T. The generated frequency tones of the radiated impulse are measured at the harmonics of 5.2 GHz, from 50 GHz to 1.1 THz.

Fig. 23 shows the measured spectral line width and received signal-to-noise ratio (SNR) following down conversion. The SNR is limited by the path loss and noise figure of the down-conversion mixer. Fig. 22 shows the frequency tones measured at 1.1, 1.08, 0.9, 0.81, 0.75, and 0.6 THz. The measured received SNR in these frequencies are 20, 22, 30, 34, 40, and 40 dB, respectively. The SNR numbers reported are measured at the receiver, which is at a distance of at least

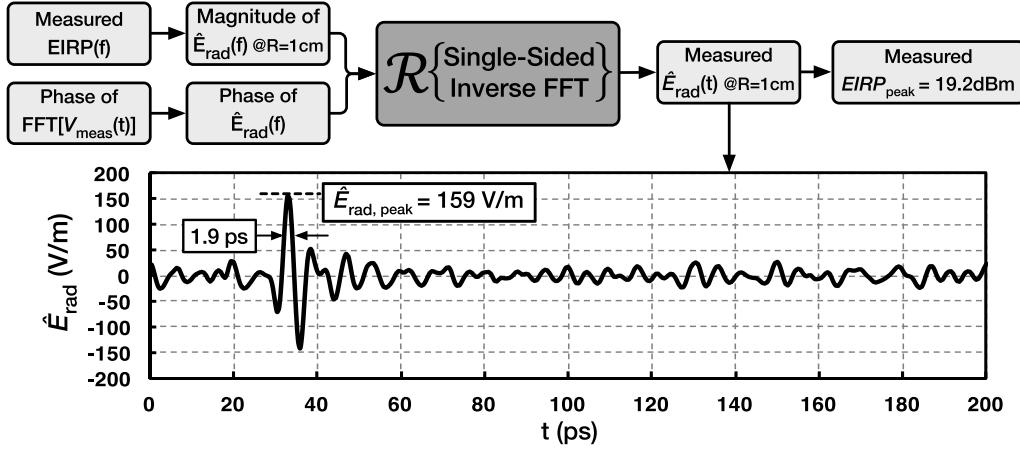


Fig. 25. Illustration of the method used to acquire the measured  $E$ -field at a distance of 1 cm and a peak pulse EIRP of 19.2 dBm.

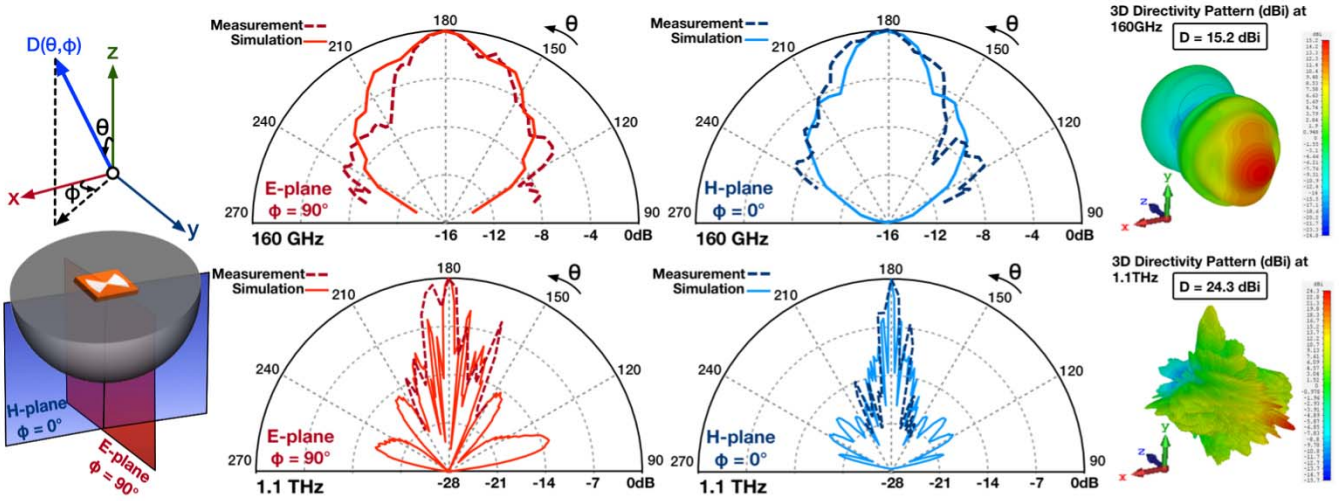


Fig. 26. Frequency-domain radiation patterns at 160 GHz (center frequency of the pulse) and 1.1 THz (highest frequency measured) in simulation and measurement.

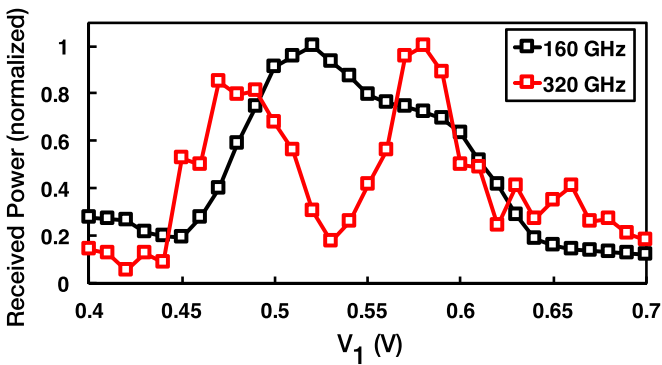


Fig. 27. Measured received power at 160 and 320 GHz versus  $V_1$ .

4 cm from the chip; therefore, the SNR at the transmitter is much higher. In addition, Fig. 23 includes the measured received SNR versus frequency for a calibrated distance of 100 mm at all mixer bands.

The average EIRP spectrum of the radiator is calculated based on the frequency domain measurements for the entire 0.05–1.1 THz range and plotted against the simulation in Fig. 24. The EIRP numbers are calculated based on the Friis transmission equation. It should be noted that the numbers reported in Fig. 24 are average frequency-domain EIRP values for a pulse radiator with a 1.9-ps pulse width and a pulse-to-pulse spacing of 192 ps (5.2-GHz repetition rate). The fluctuation in the plot in Fig. 24 is due to the use of several different mixers and antennas, the filtering effect of the ON/OFF impulse-shaping technique (Section III-B), and reflections from surrounding objects.

Measurement results are used to calculate two parameters of the radiated pulses. These parameters are the peak pulse EIRP and the peak pulse radiated power. First, the peak pulse EIRP is calculated based on both the time- and frequency-domain measurement results. Fig. 24 shows the measured average EIRP spectrum. In another plot (Fig. 25), to calculate the peak pulse EIRP, an inverse FFT of the average EIRP spectrum is taken by importing the phase information from the

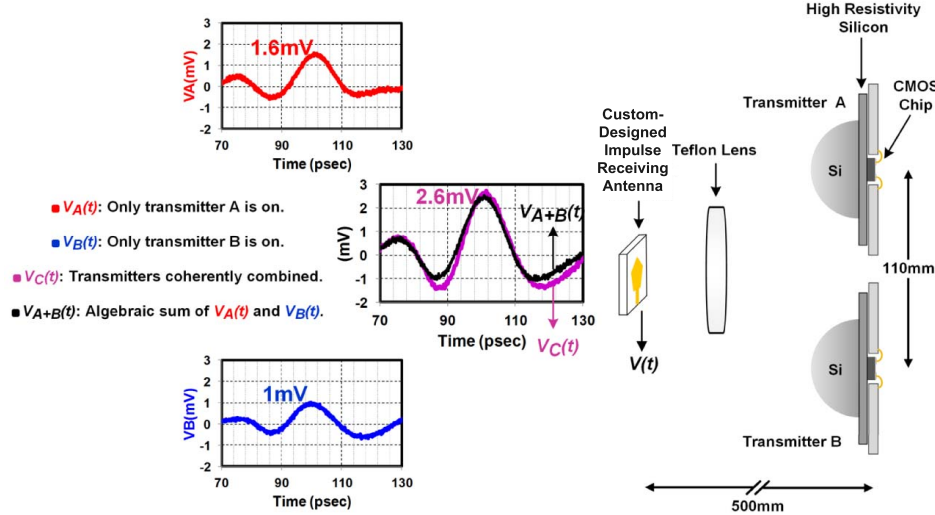


Fig. 28. Coherent spatial combining experiment from two widely spaced radiators.

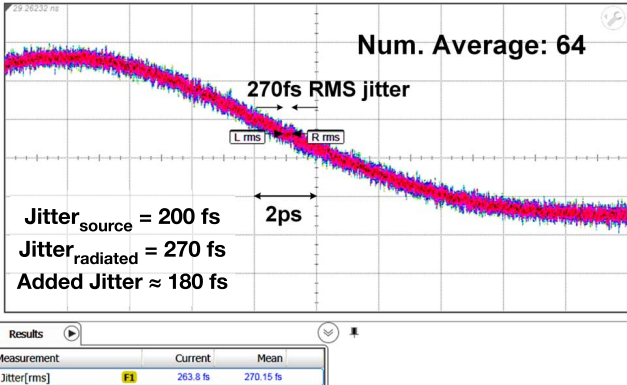


Fig. 29. Measured jitter of the combined signal.

time-domain measurement data in Section IV-A. This results in a measured time-domain  $E$ -field  $E_{\text{rad}}(t)$ . The peak value of the radiated  $E$ -field is measured 159 V/m, at an imaginary distance of 1 cm, which is used only as a reference distance. This does not mean the measurements are performed at 1 cm and it is only a reference used in the calculations. Using the distance of the virtual  $E$ -field probe from the antenna ( $R = 1$  cm), the peak of the radiated  $E$ -field in time ( $E_{\text{rad}, \text{peak}} = 159$  V/m), and the wave impedance in free space ( $\eta_0 = 377 \Omega$ ) in (6), a peak pulse EIRP of 19.2 dBm and a peak pulse radiated power of 2.6 mW are measured.

The frequency-domain radiation pattern of the THz impulse radiator chip is also measured at two frequency components: the center frequency of 160 GHz and the maximum frequency of 1.1 THz. Fig. 26 shows the measured and simulated  $E$ -plane and  $H$ -plane radiation patterns, as well as the 3-D directivity patterns at these frequencies. The antenna directivities at 160 GHz and 1.1 THz are 15.2 and 24.3 dBi, respectively. The pattern at 1.1 THz is narrower and has more lobes as expected.

*1) Impulse-Shaping Measurements:* The impulse-shaping technique is designed and employed to suppress the 30-GHz

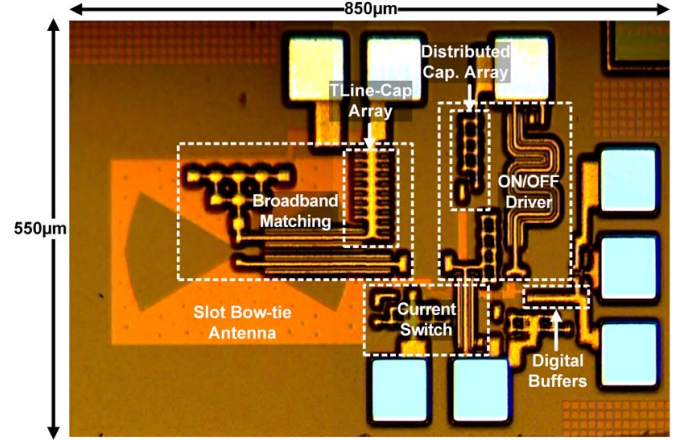


Fig. 30. Micrograph of the chip.

ringing effects. This method also significantly increases the dc-to-radiated efficiency of the current-switch by keeping the current switch OFF after turning it on for a few picoseconds. This method is not inherently designed to be used as a dynamic waveform alteration technique, however, to certain capacity, it can be used to change the center frequency of the pulses around 160 GHz. To characterize the impulse-shaping technique, the received power at 160 GHz and its second harmonic, 320 GHz, are measured versus the biasing voltage of the ON/OFF driving signal at the base of transistor  $Q_1$ ,  $V_1$ . These measurement results are shown in Fig. 27. Based on these plots, an effective  $t_d$  value can be extracted. It is concluded that at  $V_1 = 0.47$  V, a  $t_d$  value of 1.5 ps maximizes the 320-GHz component. At  $V_1 = 0.53$  V, the 160-GHz power reaches a maximum while the 320-GHz power reaches a minimum, which happens at  $t_d = 3$  ps. By increasing  $V_1$  to 0.58 V, the 320-GHz component's power reaches a maximum caused by a  $t_d$  of 4.5 ps. By further increasing  $V_1$ , both power components drop which is expected based on the filtering effect of the ON/OFF technique explained by (3)–(5). Below  $V_1 = 0.4$  V, the current switch does not turn on and

TABLE I  
PERFORMANCE SUMMARY OF THE CHIP AND COMPARISON WITH PRIOR WORK

Performance	This work	[4]	[11]	[3]	[24]	[25]
<b>Highest frequency measured with SNR &gt; 1</b>	1.1 THz (22-dB SNR)	110 GHz	214 GHz	N/A	N/A	197 GHz
<b>Shortest radiated pulse width (FWHM)</b>	1.9 ps	26 ps	2.6 ps*	60 ps	9 ps	4 ps
<b>Peak EIRP (dBm)</b>	19.2	13	-3.4	15.2	10	-9.4 (avg. EIRP)
<b>Time-domain measurement</b>	Yes (with locking)	Yes	No	Yes (with locking)	Yes (with locking)	Yes (with locking)
<b>Frequency-domain measurement</b>	Yes (up to 1.1 THz)	Yes	Yes	N/A	N/A	Yes (up to 197 GHz)
<b>Coherent spatial combining with multiple chips</b>	Performed	N/A	N/A	N/A	N/A	N/A
<b>Pulse generation method</b>	Direct digital-to-impulse (D2I)	Oscillator-based	Oscillator-based	Oscillator-based	Direct digital-to-impulse (D2I)	D2I with NLQSI
<b>Power consumption (mW)</b>	105	1400 (TX + RX)	N/A	106	260	170
<b>Die area (mm<sup>2</sup>)</b>	0.47	6.16 (TX + RX)	2.5	2.85	0.88	1
<b>Technology</b>	130-nm SiGe BiCMOS	130-nm SiGe BiCMOS	65-nm CMOS	130-nm SiGe BiCMOS	130-nm SiGe BiCMOS	130-nm SiGe BiCMOS

\* Simulated result; not a true time-domain measurement. Only two tones used.

this effect cannot be measured. A resolution of 10 mV is used to adjust  $V_1$  in these measurements.

## V. COHERENT SPATIAL COMBINING OF IMPULSES FROM WIDELY SPACED RADIATORS

Precision synchronization between the digital trigger and the radiated impulse enables coherent combining of radiated impulses from widely spaced antennas with increased effective aperture size. To demonstrate this, the radiated THz pulses from two separate widely spaced chips are combined in space. The measurement setup of this experiment is shown in Fig. 28. Due to the difficulties in the measurement of two radiators with the THz-TDS system, a custom printed circuit board-based inverted cone planar antenna is designed and used as the receiving antenna in this experiment. The receiving antenna is directly connected to a Keysight remote sampling head 86118A. Fig. 28 shows that the measured combined signal matches with the algebraic sum of the received signals radiated from individual chips. The timing jitter of the combined signal is calculated by a Keysight 86100DCA sampling oscilloscope, which results in a root mean square (RMS) jitter of 270 fs for an averaging of 64, with an RMS jitter of 200 fs for the input trigger source with the same amplitude and number of averaging (Fig. 29). The measured jitter for averaging of 256 and 512 is 220 and 130 fs, respectively.

## VI. CONCLUSION

In this paper, a fully integrated impulse radiator chip, based on a novel oscillator-free direct D2I architecture, was introduced that is capable of radiating THz pulses with FWHM of 1.9 ps and 3-dB BW of 130 GHz (10-dB BW of 200 GHz) centered at 160 GHz. The starting time of the radiated impulses is locked to the edge of the input digital trigger.

The chip fed by a stable trigger signal radiates harmonic tones up to 1.1 THz (limited by the receiver) with an ultra-high spectral purity. Broadband 0.03–1.1 THz signal generation and radiation was demonstrated with a received SNR of 22 dB at 1.1 THz, 28 dB at 1 THz, and 30 dB at 0.9 THz. A 10 dB-below-peak spectral width of just 2 Hz at 1.1 THz was measured, which shows extremely high-frequency stability. A custom time-domain THz pulse sampling system was developed based on a femtosecond-laser-based THz-TDS setup and used to measure the waveform of the radiated pulses. The chip is fabricated in a 130-nm SiGe BiCMOS process with an  $f_T$  of 200 GHz and an  $f_{max}$  of 280 GHz. Table I compares the performance of the chip with prior work. Finally, a micrograph of the chip is shown in Fig. 30, which occupies an area of 550  $\mu\text{m} \times$  850  $\mu\text{m}$  and consumes 105-mW dc power.

## REFERENCES

- [1] M. M. Assefzadeh *et al.*, “Terahertz trace gas spectroscopy based on a fully-electronic frequency-comb radiating array in silicon,” in *Proc. CLEO, Sci. Innov.*, 2016, paper SM2L-7. [Online]. Available: [https://www.osapublishing.org/abstract.cfm?uri=CLEO\\_SI-2016-SM2L7](https://www.osapublishing.org/abstract.cfm?uri=CLEO_SI-2016-SM2L7)
- [2] M. M. Assefzadeh and A. Babakhani, “Broadband THz spectroscopic imaging based on a fully-integrated 4  $\times$  2 digital-to-impulse radiating array with a full-spectrum of 0.03–1.03 THz in silicon,” in *Proc. IEEE Symp. VLSI Technol.*, Jun. 2016, pp. 1–2.
- [3] P. Chen and A. Babakhani, “A 30 GHz impulse radiator with on-chip antennas for high-resolution 3D imaging,” in *Proc. IEEE Radio Wireless Symp. (RWS)*, Jan. 2015, pp. 32–34.
- [4] A. Arbabian, S. Callender, S. Kang, M. Rangwala, and A. M. Niknejad, “A 94 GHz mm-wave-to-baseband pulsed-radar transceiver with applications in imaging and gesture recognition,” *IEEE J. Solid-State Circuits*, vol. 48, no. 4, pp. 1055–1071, Apr. 2013.
- [5] S. Koenig *et al.*, “Wireless sub-THz communication system with high data rate,” *Nature Photon.*, vol. 7, no. 12, pp. 977–981, Dec. 2013.
- [6] J. M. Jornet and I. F. Akyildiz, “Femtosecond-long pulse-based modulation for terahertz band communication in nanonetworks,” *IEEE Trans. Commun.*, vol. 62, no. 5, pp. 1742–1754, May 2014.

- [7] S. Matsuura, M. Tani, and K. Sakai, "Generation of coherent terahertz radiation by photomixing in dipole photoconductive antennas," *Appl. Phys. Lett.*, vol. 70, no. 5, pp. 559–561, 1997.
- [8] N. Chimot *et al.*, "Terahertz radiation from heavy-ion-irradiated In<sub>0.53</sub>Ga<sub>0.47</sub>As photoconductive antenna excited at 1.55 μm," *Appl. Phys. Lett.*, vol. 87, no. 19, p. 193510, Nov. 2005.
- [9] N. M. Froberg, B. BinHu, X.-X. Zhang, and D. H. Auston, "Terahertz radiation from a photoconducting antenna array," *IEEE J. Quantum Electron.*, vol. 28, no. 10, pp. 2291–2301, Oct. 1992.
- [10] B. Salem, D. Morris, V. Aimez, J. Beerens, J. Beauvais, and D. Houde, "Pulsed photoconductive antenna terahertz sources made on ion-implanted GaAs substrates," *J. Phys., Condens. Matter*, vol. 17, no. 46, p. 7327, 2005.
- [11] X. Wu and K. Sengupta, "Dynamic waveform shaping with picosecond time widths," *IEEE J. Solid-State Circuits*, vol. 52, no. 2, pp. 389–405, Feb. 2017.
- [12] R. M. Woodward, V. P. Wallace, D. D. Arnone, E. H. Linfield, and M. Pepper, "Terahertz pulsed imaging of skin cancer in the time and frequency domain," *J. Biol. Phys.*, vol. 29, no. 2, pp. 257–259, 2003.
- [13] E. Pickwell, B. E. Cole, A. J. Fitzgerald, M. Pepper, and V. P. Wallace, "In vivo study of human skin using pulsed terahertz radiation," *Phys. Med. Biol.*, vol. 49, no. 9, pp. 1595–1607, 2004.
- [14] H. Lin *et al.*, "Studying pharmaceutical tablet coating process with real-time terahertz in-line sensing," in *Proc. 38th Int. Conf. Infr., Millim., Terahertz Waves (IRMMW-THz)*, Sep. 2013, pp. 1–2.
- [15] M. Mohara, K. Shimura, K. Aiko, N. Shiramizu, K. Murate, and K. Kawase, "Pharmaceutical tablet inspection with injection-seeded terahertz parametric generation technique," in *Proc. 41st Int. Conf. Infr., Millim., Terahertz Waves (IRMMW-THz)*, Sep. 2016, pp. 1–2.
- [16] C. J. Strachan *et al.*, "Using terahertz pulsed spectroscopy to quantify pharmaceutical polymorphism and crystallinity," *J. Pharmaceutical Sci.*, vol. 94, no. 4, pp. 837–846, 2005.
- [17] C. D. Stoik, M. J. Bohn, and J. L. Blackshire, "Nondestructive evaluation of aircraft composites using transmissive terahertz time domain spectroscopy," *Opt. Exp.*, vol. 16, no. 21, pp. 17039–17051, Oct. 2008.
- [18] Y. C. Shen and P. F. Today, "Development and application of terahertz pulsed imaging for nondestructive inspection of pharmaceutical tablet," *IEEE J. Sel. Topics Quantum Electron.*, vol. 14, no. 2, pp. 407–415, Mar. 2008.
- [19] C. Baker, T. Lo, W. R. Tribe, B. E. Cole, M. R. Hogbin, and M. C. Kemp, "Detection of concealed explosives at a distance using terahertz technology," *Proc. IEEE*, vol. 95, no. 8, pp. 1559–1565, Aug. 2007.
- [20] J. Chen, Y. Chen, H. Zhao, G. J. Bastiaans, and X.-C. Zhang, "Absorption coefficients of selected explosives and related compounds in the range of 0.1–2.8 THz," *Opt. Exp.*, vol. 15, no. 19, pp. 12060–12067, 2007.
- [21] H.-B. Liu, H. Zhong, N. Karpowicz, Y. Chen, and X.-C. Zhang, "Terahertz spectroscopy and imaging for defense and security applications," *Proc. IEEE*, vol. 95, no. 8, pp. 1514–1527, Aug. 2007.
- [22] G. Marconi, "Wireless telegraphy," *J. Inst. Elect. Eng.*, vol. 28, no. 139, pp. 273–290, Apr. 1899.
- [23] M. M. Assefzadeh and A. Babakhani, "An 8-psec 13 dBm peak EIRP digital-to-impulse radiator with an on-chip slot bow-tie antenna in silicon," in *IEEE MTT-S Int. Microw. Symp. Dig.*, Jun. 2014, pp. 1–4.
- [24] M. M. Assefzadeh and A. Babakhani, "A 9-psec differential lens-less digital-to-impulse radiator with a programmable delay line in silicon," in *IEEE Radio Freq. Integr. Circuits Symp. Dig. Tech. Papers*, Jun. 2014, pp. 307–310.
- [25] P. Chen, M. M. Assefzadeh, and A. Babakhani, "A nonlinear Q-switching impedance technique for picosecond pulse radiation in silicon," *IEEE Trans. Microw. Theory Techn.*, vol. 64, no. 12, pp. 4685–4700, Dec. 2016.
- [26] D. F. Filipovic, S. S. Gearhart, and G. M. Rebeiz, "Double-slot antennas on extended hemispherical and elliptical silicon dielectric lenses," *IEEE Trans. Microw. Theory Techn.*, vol. 41, no. 10, pp. 1738–1749, Oct. 1993.
- [27] A. Babakhani, G. Xiang, A. Komijani, A. Natarajan, and A. Hajimiri, "A 77-GHz phased-array transceiver with on-chip antennas in silicon: Receiver and antennas," *IEEE J. Solid-State Circuits*, vol. 41, no. 12, pp. 2795–2806, Dec. 2006.
- [28] S.-W. Qu, J.-L. Li, Q. Xue, and C. H. Chan, "Wideband cavity-backed bowtie antenna with pattern improvement," *IEEE Trans. Antennas Propag.*, vol. 56, no. 12, pp. 3850–3854, Dec. 2008.
- [29] Y.-L. Chen, C.-L. Ruan, and L. Peng, "A novel ultra-wideband bow-tie slot antenna in wireless communication systems," *Prog. Electromagn. Res. Lett.*, vol. 1, pp. 101–108, 2008. [Online]. Available: <http://www.jpier.org/pier/pier.php?paper=07112302>, doi: 10.2528/PIERL07112302.
- [30] N. Engheta, C. H. Papas, and C. Elachi, "Radiation patterns of interfacial dipole antennas," *Radio Sci.*, vol. 17, no. 6, pp. 1557–1566, 1982.
- [31] K. V. Shrikhande, A. L. Lentine, M. C. Nuss, H. Kogelnik, and A. V. Krishnamoorthy, "Fiber-to-the-home/desktop using Ethernet," in *Int. Conf. Integr. Opt. Opt. Fiber Commun. (OFC/IOOC) Dig. Tech. Paper*, vol. 2, 1999, pp. 353–355.
- [32] N. G. Alexopoulos, P. B. Katehi, and D. B. Rutledge, "Substrate optimization for integrated circuit antennas," *IEEE Trans. Microw. Theory Techn.*, vol. MTT-31, no. 7, pp. 550–557, Jul. 1983.
- [33] B. Chantraine-Bares, R. Sauleau, L. L. Coq, and K. Mahdjoubi, "A new accurate design method for millimeter-wave homogeneous dielectric substrate lens antennas of arbitrary shape," *IEEE Trans. Antennas Propag.*, vol. 53, no. 3, pp. 1069–1082, Mar. 2005.
- [34] T. Nagatsuma *et al.*, "Millimeter-wave photonic integrated circuit technologies for high-speed wireless communications applications," in *Proc. IEEE Int. Solid-State Circuits Conf.*, vol. 1, Feb. 2004, pp. 448–449.
- [35] K. Chung, S. Pyun, and J. Choi, "Design of an ultrawide-band TEM horn antenna with a microstrip-type balun," *IEEE Trans. Antennas Propag.*, vol. 53, no. 10, pp. 3410–3413, Oct. 2005.



**M. Mahdi Assefzadeh** (S'14) received the B.S. degree in electrical engineering from the Sharif University of Technology, Tehran, Iran, in 2011, and the M.S. degree in electrical engineering from Rice University, Houston, TX, USA, in 2014, where he is currently pursuing the Ph.D. degree.

Mr. Assefzadeh was a recipient of numerous awards, including the Best Paper Award of the IEEE MTT-S International Microwave Symposium in 2014, the Best Paper Award of the IEEE Radio and Wireless Symposium in 2016, the Second Place of the Best Paper Award at the IEEE Antenna and Propagation Symposium in 2016, and the Runner-Up at the Best Paper Award of IRMMW-THz 2016. He was a recipient of the IEEE MTT-S Microwave Graduate Fellowship in 2017, the Texas Instruments Distinguished Fellowship in 2012, and the Michael and Katherine Birck Fellowship of Purdue University in 2011. He was also the Gold Medal recipient at the National Physics Competition in 2006 and the 38th International Physics Olympiad in 2007.



**Aydin Babakhani** (M'08) received the B.S. degree in electrical engineering from the Sharif University of Technology, Tehran, Iran, in 2003, and the M.S. and Ph.D. degrees in electrical engineering from the California Institute of Technology, Pasadena, CA, USA, in 2005 and 2008, respectively.

In 2009, he was a Post-Doctoral Scholar with the California Institute of Technology and in 2010, he was a Research Scientist with the IBM Thomas J. Watson Research Center, Yorktown Heights, NY, USA. From 2011 to 2016, he was an Assistant Professor of electrical and computer engineering with Rice University, Houston, TX, USA, where he was a Louis Owen Junior Chair Assistant Professor from 2016 to 2017. He is currently an Associate Professor with the Department of Electrical and Computer Engineering, Rice University, and the Director of the Rice Integrated Systems and Circuits Laboratory. He is a Co-Founder of MicroSilicon Inc, Houston, TX, USA. He has authored or co-authored more than 85 papers in peer-reviewed journals and conference proceedings, and holds 21 issued or pending patents. His research has been supported by the NSF, DARPA, AFOSR, ONR, the W. M. Keck Foundation, SRC, and more than ten companies.

Dr. Babakhani is a Member of the DARPA Microsystems Exploratory Council. He was a recipient of numerous awards including the Best Paper Award of the IEEE Silicon Monolithic Integrated Circuits in RF Systems Conference in 2016, the Best Paper Award of the IEEE Radio and Wireless Symposium in 2015, the Best Paper Award of the IEEE MTT-S International Microwave (IMS) Symposium in 2014, and second place of the Best Paper Award of the IEEE International Symposium on Antennas and Propagation Symposium 2016 and the IEEE MTT-S IMS Symposium 2016. He was a recipient of the prestigious NSF CAREER Award in 2015, the Innovation Award from Northrop Grumman in 2014, the DARPA Young Faculty Award in 2012, the California Institute of Technology Electrical Engineering Department's Charles Wilts Best Ph.D. Thesis Prize for his work entitled "Near-Field Direct Antenna Modulation," the Microwave Graduate Fellowship in 2007, the Grand Prize in the Stanford-Berkeley-Caltech Innovators Challenge in 2006, and the Analog Devices Inc. Outstanding Student Designer Award in 2005, as well as a California Institute of Technology Special Institute Fellowship and an Atwood Fellowship in 2003. He was also the Gold Medal recipient at both the National Physics Competition in 1998 and the 30th International Physics Olympiad in Padova, Italy, in 1999.